SSRG International Journal of Electrical and Electronics Engineering
ISSN: 2348-8379/ https://doi.org/10.14445/23488379/IJEEE-V11I3P103

Volume 11 Issue 3, 25-41, March 2024

Original Article

Improved KY Buck-Boost Converter with Meta-Heuristic Optimization for HRES Based EV-Charging

K.S.V.V. Prasada Rao[1], M. Anitha[2], V. Srinivasa Rao[3]

[1]*Department of Electrical and Electronics Engineering, Annamalai University, Tamil Nadu, India*
[2]*Department of Electrical Engineering, Annamalai University, Tamil Nadu, India.*
[3]*Department of Electrical and Electronics Engineering, Aditya Engineering College (A), Andhra Pradesh, India.*

[1]*Corresponding Author : ksvvprasadarao@gmail.com*

Received: 03 January 2024 Revised: 03 February 2024 Accepted: 01 March 2024 Published: 25 March 2024

Abstract *- As a non-polluting alternative to fuel-based vehicles, Electric Vehicles (EVs) are an advantageous choice. Electricity is typically required to charge these EVs; hence, a novel Renewable Energy Source (RES) powered EV charging station connected to the grid is developed. EV charging stations are required where energy for charging is sourced from RES because the energy stored in EV batteries is insufficient for long-distance driving. This work puts forth the proposal of Hybrid Renewable Energy Source (HRES)-based EV charging, in which these charging stations are equipped with RES and battery storage systems. The energy produced from the PV panel is supplied to the grid via an improved KY buck-boost converter along with a Three Phase Voltage Source Inverter (3ϕ VSI). The energy obtained is additionally stored in an EV battery for further use. By resolving optimization issues and accelerating convergence, the Sea Lion Optimized PI controller (SLnO-PI), which controls converter operation, maintains a steady supply to the DC link. Similarly, by using a Proportional Integral (PI) controller, 3ϕ VSI coupled to the grid is maximized. The Pulse Width Modulation (PWM) rectifier, which is utilized in Wind Energy Conversion Systems (WECS) employing a Doubly Fed Induction Generator (DFIG), converts AC to DC with the help of a PI controller. The work is simulated in MATLAB Simulink software and respective outcomes are obtained and outcomes are analyzed with efficiency of 97% and voltage gain of 1:16.*

Keywords *- EV, HRES, KY buck-boost converter, DFIG, WECS, MATLAB.*

1. Introduction

Increasing fossil fuel prices and updated regulations aiming at decreasing CO_2 emissions in traditional automobiles have prompted interest in EVs. It requires excellent charging stations to “refuel” the batteries on a frequent basis to run smoothly and continuously [1, 2].

The instantaneous connecting of several EVs to an electrical grid for charging enhances the demand for power and causes other grid-related challenges. Using energy from RES for EV charging represents a particular response to power system challenges. Because of the benefits it offers, solar PV power generation is preferable to other RESs. Electricity for EVs is produced pollution-free by solar-powered charging stations, which is good for the environment [3, 4]. Because of the steady drop in PV module prices, PV is becoming increasingly regarded as a competitive energy source for grid supplementation [5].

Furthermore, PV system requires minimal repairs in terms of workforce and fuel. Energy exchanging technology, battery management systems, improved installation procedures, and design standards have all contributed to a considerable improvement in the application of PV to charge EVs [6].

As a result, a step-up gain DC-DC converter is employed to enhance the low direct voltage obtained from the PV system in order to meet the power equipment’s requirements. The Boost converter [7] lacks current input control, yet it is capable of providing high gain at low-duty ratios. At a high-duty cycle, it draws some input current from the source, causing problems with converter parts.

Buck converters, Buck-boost converters [8], Cuk converters [9, 10], Zeta [11] and Single-Ended Primary Inductance Converters (SEPIC) [12, 13] are examples of conventional single switch step-down/step-up converters. These converters are preferably used for converting low DC output voltage to high DC output voltage.

Even though Buck-boost and Cuk converters step voltages up and down, their efficiency is insufficient, causing stress on the component. KY converter has low voltage ripples

and quick transient response to achieve maximum power point. It is utilized in photovoltaic systems that operate in Continuous Conduction Mode (CCM) to overcome the complexity due to output ripple waves and voltage transfer gain [14].

Still, it causes leakage inductance loss, reducing the converter's capacity. To manage the output voltage of the KY buck-boost converter [15], a simple voltage-controlled analog regulator is proposed in this study. KY buck-boost converter produces output voltage with precisely the same polarity as the input voltage. In this work, an improved KY buck-boost converter is proposed to improve the voltage obtained from the PV system. Following the converter operation, a controller approach is used to compensate for energy obtained from the PV system. PI controller is a technology that is widely used to extract additional power from a solar system [16].

Genetic Algorithm (GA) is a population-based algorithm that employs the concepts of biological evolution and survival of the fittest. Because the significant GA operators are selection, crossover, and mutation [17], the iteration process is exceedingly slow and difficult to understand and debug. The Grey Wolf Optimization (GWO) algorithm [18] takes into account the grey wolves' hunting behaviour and leadership structure. Although it is straightforward to build with fewer parameters, its performance is hampered by poor speed of convergence and low solution accuracy.

The particle Swarm Optimization (PSO) algorithm [19] makes use of sharing information and collaboration among individuals to find the best solution; each particle updates its velocity and position in every iteration by analyzing the individual highest values and global extreme values.

However, it has a slow convergence speed during the process of iteration. In this work, the SLnO method, a unique metaheuristic optimization system that mimics the hunting behaviour of sea lions, is proposed. The results reveal that the SLnO method outperforms other standard metaheuristic algorithms.

The Wind turbine linked to DFIG is the most commonly used form of WECS technology due to its lower converter ratings and adequate power consumption due to variable speed operation. The DFIG is used in the majority of existing wind turbines, accounting for around half of all installations. Because it makes excellent use of the rotor core, DFIG provides tremendous torque and small size [20, 21].

The PI controller controls the VSI, which is used for effective grid synchronization and increased reactive power adjustment. The LC filter [22] is employed to minimize the harmonics generated by the system, thereby improving the stability of the system. The contributions made in this work are listed below,

- ❖ Implementing a novel improved KY buck-boost converter to step up/down the voltage obtained from the PV system.
- ❖ Sustaining a steady direct voltage throughout the system using SLnO assisted PI controller.
- ❖ Implementing the PI controller to stabilize output from the DFIG-based WECS.
- ❖ Integrating grid synchronization with PI controllers to ensure uninterrupted power supplies for EV charging.

The overall system is executed in MATLAB software to verify its effectiveness in HRES-based EV charging.

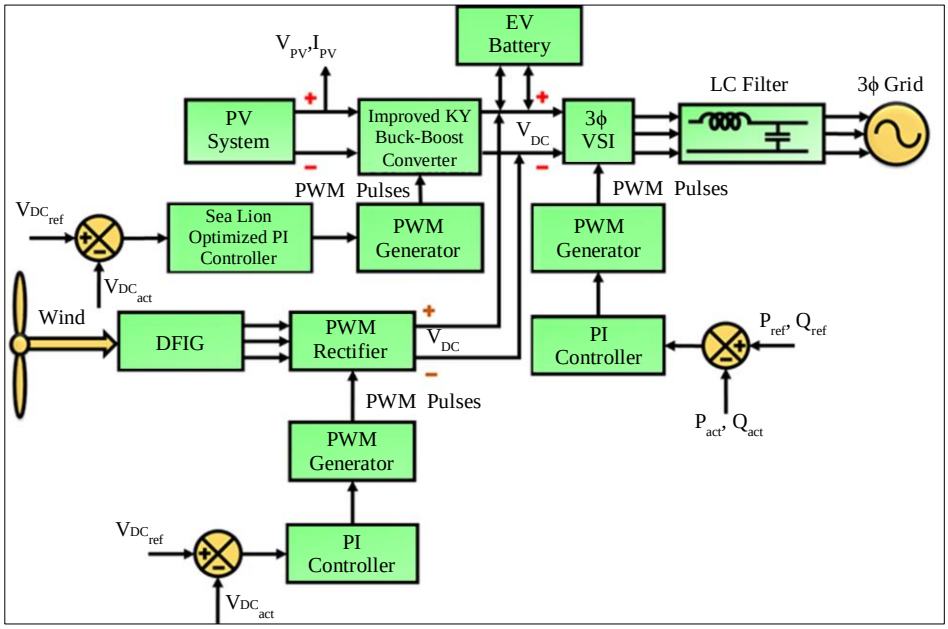

Fig. 1 Schematic diagram for HRES-based EV charging

2. Proposed System Description

EV is able to be charged from renewable energy sources by storing wind power at night and solar electricity during the day, which encourages the development of clean energy and reduces emissions of greenhouse gases. A hybrid renewable source is integrated into the grid with an improved KY buck-boost converter proposed with an SLnO-PI controller, which is synchronized with the grid through a 3ϕ VSI control scheme, as shown in Figure 1.

The electricity that comes out of the PV system is influenced by solar irradiation and temperature variations, resulting in a low direct voltage. As a result, the converter is necessary for improving direct voltage to a more significant amount. In this proposed work, an improved KY buck-boost converter is utilized to enhance the direct voltage obtained from the PV system. In this proposed system, an SLnO-based PI controller is used for maximizing the PI parameters by comparing. V_(DC ref) and V_(DC act), through which PWM pulses are engendered for better working of Improved KY buck-boost converter.

The wind energy fed into the DFIG is provided to a PWM rectifier, and the resulting value is delivered to the grid through a 3ϕ VSI, which leads to DC-AC conversion. For the purpose of synchronizing the electrical supply with the grid, PWM pulses are generated, which are then sent to VSI through the PI controller by analyzing P_ref, Q_ref with P_act, Q_ref resulting in reactive power compensation and grid synchronization.

3. Proposed System Modelling

3.1. PV System Modelling

Photovoltaic systems use semiconducting components to convert solar energy into direct electricity. A photovoltaic system uses solar panels, which are composed of various solar cells, to produce the necessary solar energy. When modelling this system, irradiance and temperature are crucial variables to take into account.

A PV system's output voltage fluctuates as a result of variations in temperature and irradiance. In order to effectively reduce oscillation and increase solar output power, an upgraded KY-Boost converter is utilized in this work. Figure 2 shows the PV module's circuit arrangement.

The PV module's current flow is expressed as,

$$I = I_{ph} - I_o\left[e^{\frac{(V+R_sI)}{V_k\alpha}-1}\right] - \frac{V+IR_s}{R_{sh}} \quad (1)$$

Where V_k represents maximum thermal voltage, I_o denotes PV current, α indicates ideality constant for diode, I_{ph} denotes input photocurrent, R_s and R_{sh} represents the series and shunt resistance, respectively, I_d represents diode current, V denotes PV voltage, and I means the output PV current. The output received from the PV system is low, which is then fed into an improved KY buck-boost converter for stepping up or down the voltage obtained.

3.2. Improved KY Buck-Boost Converter

Voltage received from the PV system is intermittent; therefore, a converter approach is required to improve the obtained PV voltage. Figure 3 represents the circuit diagram for the improved KY buck-boost converter, and Figure 5 indicates the converter operation diagram. This combines a synchronous Buck and Boost converter, which is made up of power switch S, capacitor C_1, C_2 andC_3, inductor L_1, L_2 and L_3 with a standard output load R_0.

3.2.1. Mode 1

In this phase, switch S is kept ON, and diode D is kept OFF, in which input voltage supplies energy to C_1 and L_1, causing C_1 to charge and L_1 to magnetize, as shown in Figure 4(a). Simultaneously, input voltage, in conjunction with capacitor C_2, delivers energy to the inductor L_2 and output, causing C_2 to lose its charge and L_2 to magnetize. The following equations are related to mode 1,

$$v_{L1} = V_{in} - v_{C1} \quad (2)$$

$$v_{L2} = V_{in} + v_{C2} - V_o \quad (3)$$

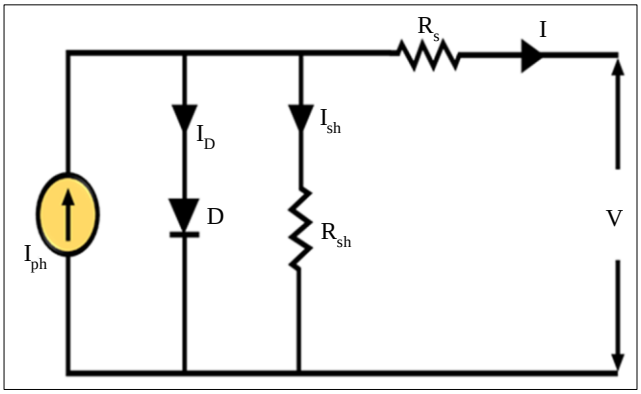

Fig. 2 PV cell model

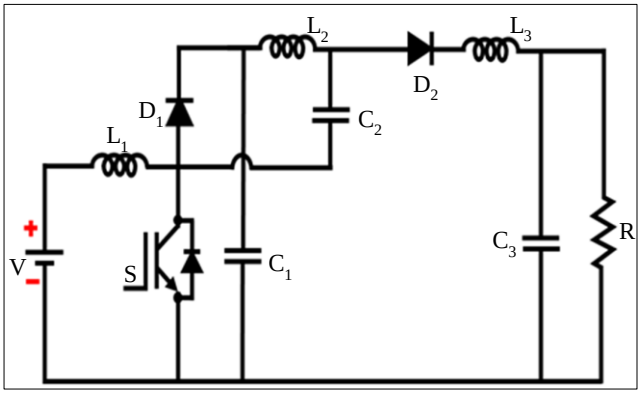

Fig. 3 Improved KY buck-boost converter

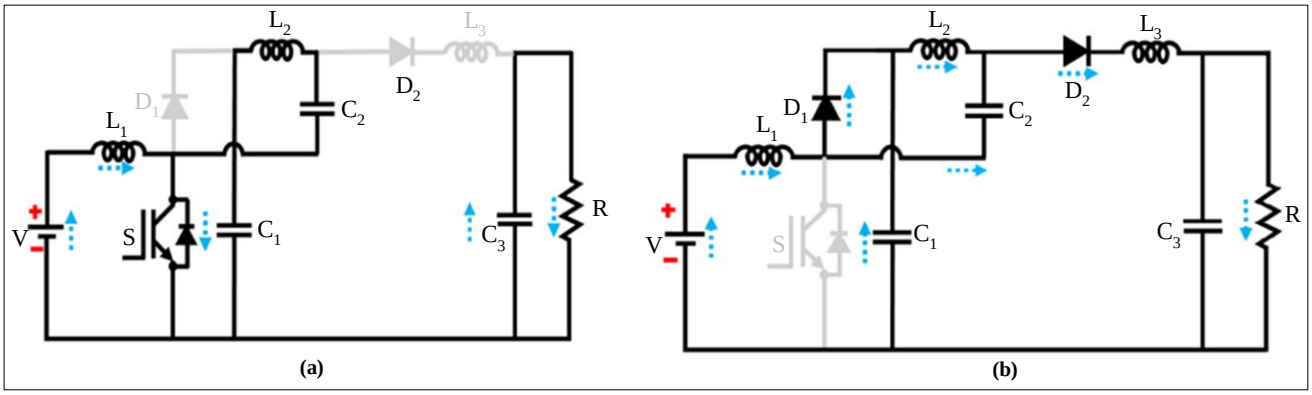

Fig. 4 Modes of operation (a) Mode 1, and (b) Mode 2.

3.2.2. Mode 2

The switch S is kept in OFF condition, and diode D is in ON condition, in which energy that is retained in inductor L_1 and capacitor C_1 is discharged to the capacitor C_2 and output via inductor L_2, producing C_1 to be discharged and L_1 to demagnetize as shown in Figure 4(b). Simultaneously, the voltage across L_2 equals v_{C2} minus V_o, which charges C_2 and demagnetizes L_2. Equations related to mode 2 are listed below;

$$v_{L1} = -v_{C1} \tag{4}$$

$$v_{L2} = v_{C2} - V_o \tag{5}$$

$$v_{c1} = v_{C2} \tag{6}$$

The equilibrium state DC voltages across C_1 and C_2 are given by,

$$v_{C1} = v_{C2} = 0.5V_0 \tag{7}$$

When compared to the input voltage, the produced voltage is greater, and it provides less voltage ripple, fast transient load response and high accurateness. In addition, because this type of converter is simple to develop and regulate, it is applicable in manufacturing environments. The following describes the optimum mechanism for control of the converter employed in this work.

3.3. Sea Lion Optimized PI Controller

The two phases of the Sea Lion algorithm, which is an optimization method based on the behaviours of sea lions when hunting, are exploration (seeking) and exploitation (attacking). Interesting traits of sea lions include their rapid movements, keen vision, and excellent hunting skills. Below are the main phases of sea lion hunting activities;

- They track and pursue the prey using their whiskers.
- Alerting other group members who had joined their subgroup while chasing and surrounding the prey.
- Going after the prey.

As they draw closer to their desired prey, sea lions make the following movements:

$$\overrightarrow{J(t+1)} = \overrightarrow{M(t)} - \overrightarrow{Dis} \cdot \vec{H} \tag{8}$$

Where, $\vec{M}(t)$ indicates the target prey's position vector, $\vec{J}(t)$ indicates the sea lion's position vector and $\overrightarrow{Dis}$ indicates the sea lion's distance from its intended prey.

Equation (9) states distance between a sea lion and its intended prey is given as,

$$(Dis)^{\rightarrow} = |2B^{\rightarrow} \cdot (J\_rand\ (t))^{\rightarrow} - (J(t))^{\rightarrow}| \tag{9}$$

Where, $B^{\rightarrow}$ indicates a random vector in the range (0,1).

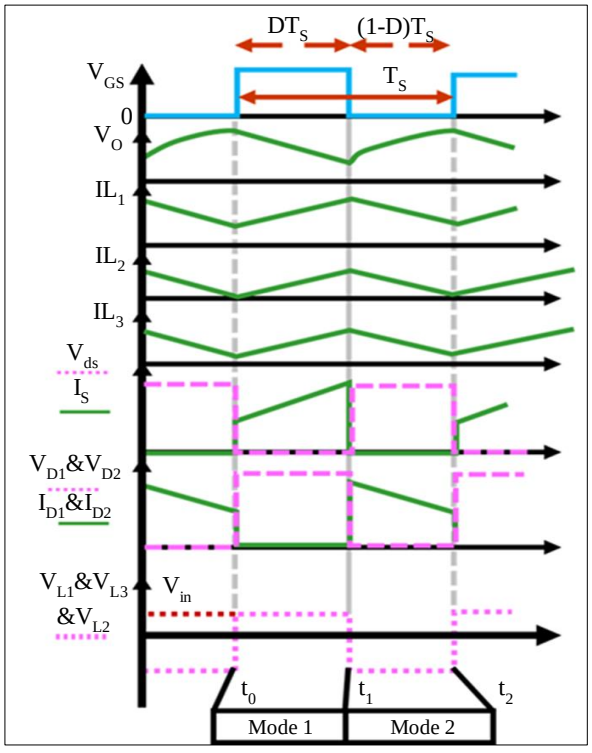

Fig. 5 Waveform for converter operation

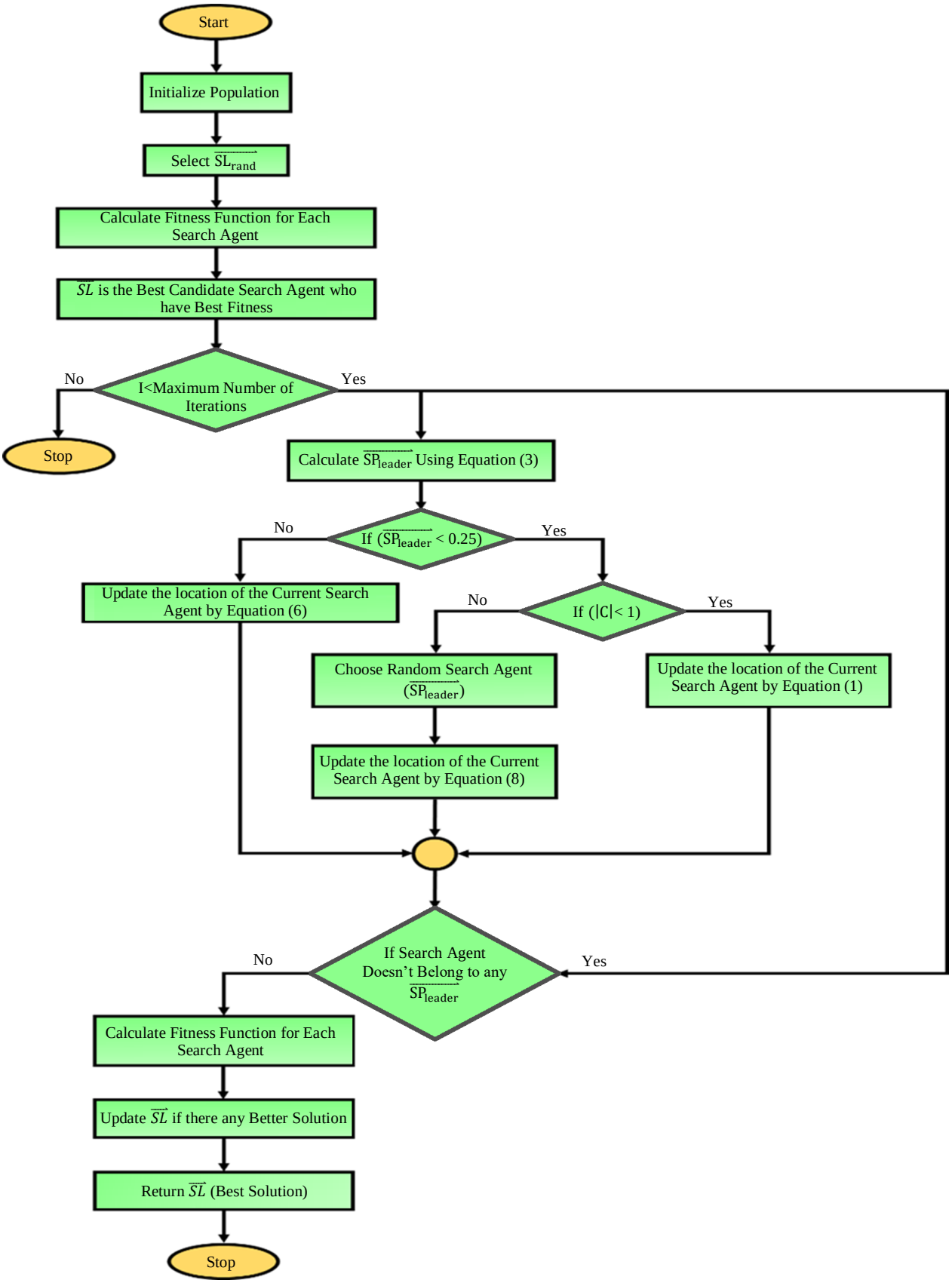

Fig. 6 Flow chart for Sea Lion algorithm

Sea lions are categorized as amphibians since they live both on land and in the water. Sea lions' vocalizations are made in such a way that sound travels four times more quickly in water than it does on land. When a sea lion spots its victim, it signals other sea lions to attack it. Figure 6 depicts the flowchart for the SLnO algorithm.

The sea lion that seeks prey is known as the leader, and the mathematical expression of its vocalization behaviour is as follows:

$$\overrightarrow{SP_{leadrer}} = \left|(\vec{V}_1(1+\overrightarrow{V_2}))/\overrightarrow{V_2}\right| \quad (10)$$

$$\overrightarrow{V_1} = sin\,\theta\ ;\ \overrightarrow{V_2} = sin\,\phi \quad (11)$$

In Equation (10), the sound speed of a sea lion is denoted as $\overrightarrow{SP_{leadrers}}$ and speed of sound in water and air of sea lion is denoted as $\overrightarrow{V_1}$ and $\overrightarrow{V_2}$ correspondingly.

Sea lions locate their prey and surround it during exploitation. Prey is referred to as the current best option, and the leader, who tells the other sea lions, is referred to as the search agent. The mathematical representation of the encircling behaviour of sea lion is given below,

$$\overrightarrow{J(t+1)} = \left|\vec{M}(t) - \vec{J}(t)\right| \cdot cos(2\pi l) + \vec{M}(t) \quad (12)$$

Where l indicates numbers chosen randomly between -1 to 1, the absolute value is denoted as $\vec{M}(t)$and the distance between the optimum solution and the search agent is indicated as $\left|\vec{M}(t) - \vec{J}(t)\right|$. The mathematical expression for sea lion hunting behaviour is $\cos(2\pi l)$, because it is circular.

According to Equation (13), the search agent's location is justified in accordance with a sea lion chosen at random and is written as,

$$\overrightarrow{J(t+1)} = \overrightarrow{J_{rnd}(t)} - \overrightarrow{D\imath s} \cdot \vec{H} \quad (13)$$

Where, $\vec{H}$ stands for limitation, which gradually drops from 2 to 0 and $\overrightarrow{J_{rnd}}$ represents a random search agent.

3.4. Modelling of Wind Power

The following Equation (14) indicates the power generated by wind.

$$P_\omega = \frac{1}{2}\pi\rho R^2 V_\omega^3 C_p(\lambda,\beta) \quad (14)$$

Where, R denotes the radius of the rotor blade, ρ indicates the density of air, β denotes the pitch angle of the blade, C_P denotes coefficient performance, λ denotes the ratio of tip speed, and V_ω denotes the velocity of wind. Equation (15) states further expression of C_p,

$$C_p(\lambda,\beta) = \frac{1}{2}(\lambda - 0.022\beta^2 - 5.6)e^{-0.17\lambda} \quad (15)$$

$$\lambda = \frac{\omega_r R}{V_\omega} \quad (16)$$

Where mechanical blade angular velocity is represented as ω_r.

3.5. DFIG Modelling

Park's model is very beneficial and popular for modelling DFIG and features a stator-oriented frame of reference. The reference frame is designed specifically for DFIG and is highly helpful for figuring out DFIG operations in both normal and fault situations the following expressions are adopted for motor convention to state stator and rotor voltages in abc frame.

$$\overrightarrow{u_s} = R_s\overrightarrow{\imath_s} + \frac{d}{dt}\overrightarrow{\lambda_s} \quad (17)$$

$$\overrightarrow{u_r} = R_r\overrightarrow{\imath_r} + \frac{d}{dt}\overrightarrow{\lambda_r} - j\omega_m\overrightarrow{\lambda_r} \quad (18)$$

The possible expressions for the fluxes triggered in the stator and rotor are given in (19):

$$\overrightarrow{\lambda_s} = L_s\overrightarrow{\imath_s} + L_m\overrightarrow{\imath_r} \quad (19)$$

$$\overrightarrow{\lambda_r} = L_r\overrightarrow{\imath_r} + L_m\overrightarrow{\imath_s} \quad (20)$$

Where $\overrightarrow{\imath_r}$ and $\overrightarrow{\imath_s}$ indicates rotor and stator currents' respective space vectors, L_m indicates magnetizing inductance, $\overrightarrow{u_r}$ and $\overrightarrow{u_s}$ denotes voltage of rotor and stator space vector, $\overrightarrow{\lambda_r}$ and $\overrightarrow{\lambda_s}$ indicates rotor and stator fluxes space vector, respectively, L_r and L_s further expressed as the following,

$$L_r = L_{lr} + L_m \quad (21)$$

$$L_s = L_{ls} + L_m \quad (22)$$

Where, L_r and L_s indicates leakage inductance of the rotor and stator, respectively. Figure 7 is drawn based on Equation (21) and (22).

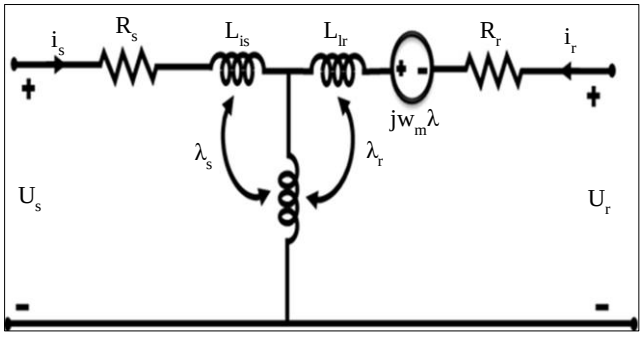

Fig. 7 DFIG equivalent circuit model

By expanding (19) and (20), the following expression is obtained,

$$\overrightarrow{\lambda_r} = \frac{L_m}{L_s}\overrightarrow{\lambda_s} - \sigma L_r \overrightarrow{i_r} \quad (23)$$

$$Where, \sigma = 1 - \frac{L_m^2}{L_s L_m} \quad (24)$$

The value of $\overrightarrow{\lambda_r}$ is replaced as follows,

$$\overrightarrow{u_r} = \frac{L_m}{L_s}\left(\frac{d}{dt} - j\omega_m\right)\overrightarrow{\lambda_s} + \left(R_r + \sigma L_r\left(\frac{d}{dt} - j\omega_m\right)\right)\overrightarrow{i_r} \quad (25)$$

By putting $\overrightarrow{i_r} = 0$ in (25), the open circuit voltage of the rotor is obtained as,

$$\overrightarrow{u_{r0}} = \frac{L_m}{L_s}\left(\frac{d}{dt} - j\omega_m\right)\overrightarrow{\lambda_s} \quad (26)$$

Both the transient reactance and rotor resistance are insignificant and negligible, the right side of Equation (25) is less when compared to $\overrightarrow{u_{r0}}$. Hence, $\overrightarrow{u_{r0}}$ is written as,

$$\overrightarrow{u_{r0}} = j\omega_r \frac{L_m}{L_s}\overrightarrow{\lambda_s} = \frac{L_m}{L_s}\frac{\omega_r}{\omega_s}U_s e^{j\omega_s t} \quad (27)$$

Where ω_s and ω_r indicates angular and synchronous frequencies of slip correspondingly. The magnitude of $\overrightarrow{u_{r0}}$ is obtained as,

$$U_{r0} = j\frac{\omega_r}{\omega_s}U_s = \frac{L_m}{L_s}sU_s \quad (28)$$

Where the value of the slip is expressed as,

$$s = \frac{\omega_s - \omega_m}{\omega_s} \quad (29)$$

$$\omega_r = \omega_s - \omega_m \quad (30)$$

From the equations mentioned above, it is evident that rotor voltage is proportional to slip and stator voltage.

3.6. Grid Synchronization

An inverter maintains DC-link voltage at a reference value while maintaining the output current's frequency and phase at grid voltage. The PI current control approach used in this work, as seen in Figure 8, uses a synchronous rotating frame mechanism to convert the three-phase symmetric grid voltage and current into DC variables and a two-phase rotating (d-q) frame to achieve sinusoidal control of the inverter.

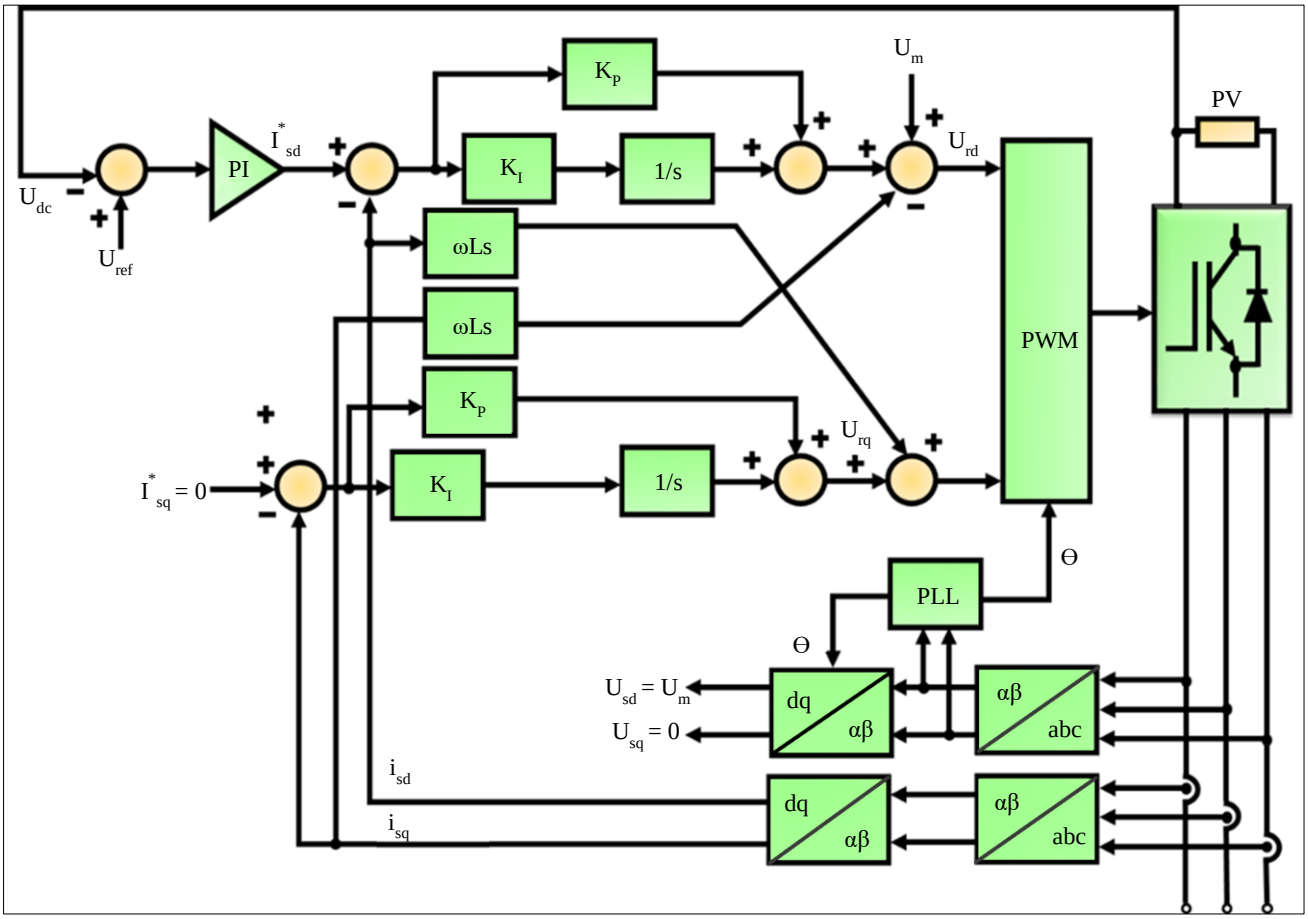

Fig. 8 Schematic diagram for grid-connected 3ϕ VSI

As a result, the current loop adopts the PI controller, realizing no steady-state error correction.The grid voltage is written as,

$$\begin{cases} u_{sa} = u_m \sin \omega t \\ u_{sb} = u_m \sin(\omega t - 2\pi/3 \\ u_{sc} = u_m \sin(\omega t + 2\pi/3 \end{cases} \quad (31)$$

From the transformation of $T_{\alpha\beta/abc}$ and $T_{dq/\alpha\beta}$, the above Equation is derived as,

$$\begin{bmatrix} u_{sd} \\ u_{sq} \end{bmatrix} = \begin{bmatrix} \cos \omega t & \sin \omega t \\ -\sin \omega t & \cos \omega t \end{bmatrix} \frac{2}{3} \begin{bmatrix} 1 & -\frac{1}{2} & -\frac{1}{2} \\ 0 & \frac{\sqrt{3}}{2} & -\frac{\sqrt{3}}{2} \end{bmatrix} \begin{bmatrix} u_{sa} \\ u_{sb} \\ u_{sc} \end{bmatrix} = \begin{bmatrix} u_m \\ 0 \end{bmatrix} \quad (32)$$

According to (32), in a synchronous rotating frame, u_{sq} and u_{sd} are DC variables; consequently, it can utilize two PI adjusters to manage reference current tracking.

4. Results and Discussion

This work describes an improved KY buck-boost converter technique for increasing PV system production. As a result, the SLnO-based PI controller linked to the PWM generator supplies controlled voltage to the DC connection. Through the PI controller, 3ϕ VSI maintains switching operation. The final system approach is implemented in MATLAB, and outcomes for simulation are obtained. Table 1 lists the parameter specifications that the proposed system makes use of.

4.1. Case 1: Variation in Temperature and Constant Intensity

The waveforms for temperature & irradiance of solar panels are depicted in Figure 9, in which temperature is continued constant at 25℃ initially, and there is a gradual change in temperature in this case 1.

Finally, it is maintained constant at 35℃ after 0.1s, as shown in Figure 9(a). The waveform for solar irradiation is represented in Figure 9(b), which shows that intensity does not vary and it is sustained at 1000W/sq-m.

Figure 10 shows the input voltage and current waveforms of the solar panel. As can be seen in Figure 10(a), the voltage is kept steady at 95V for 0.1 seconds, after which it slightly increases to 98V, which is kept constant throughout the system.

The waveform for solar panel current is shown in Figure 10(b), in which the current is raised above 15A and it gets fluctuates due to climatic conditions.

Table 1. Parameter specifications

Parameters	Specifications
Solar PV System	
Capacity	500W
Peak Power	7.5kW
No. of Panels	15
Electron Charge (q)	1.6 x 10^{-19} Coulomb
WECS	
Voltage	575V
Power	1.5kW
Improved KY Buck-Boost Converter	
Capacitor C_1 C_2 C_3	 470µF 210µF 45µF
Inductor L_1 L_2 L_3	 3000µH 1500µH 1350µH
Switching Frequency	10kHz

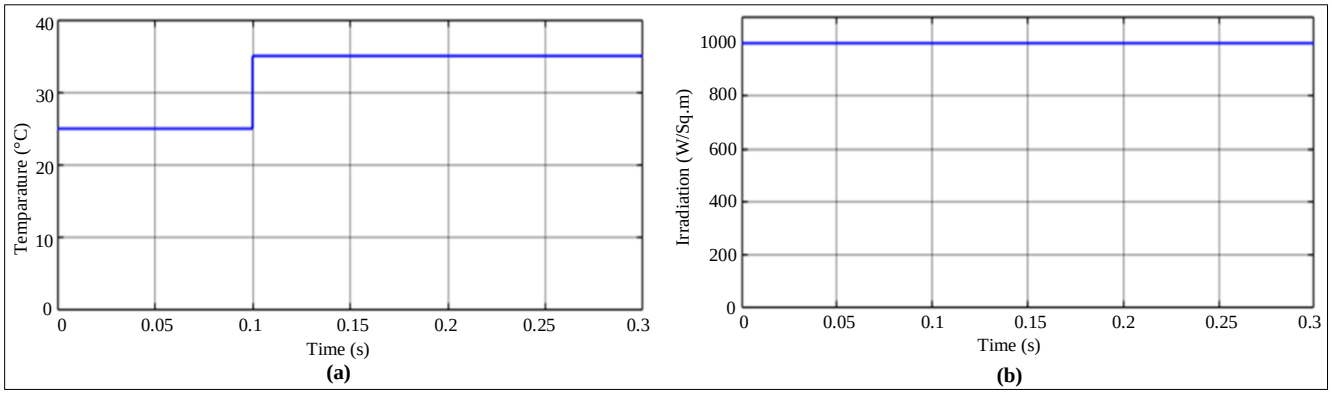

Fig. 9 Solar panel waveforms (case 1) (a) Varying temperature, and (b) Constant irradiation.

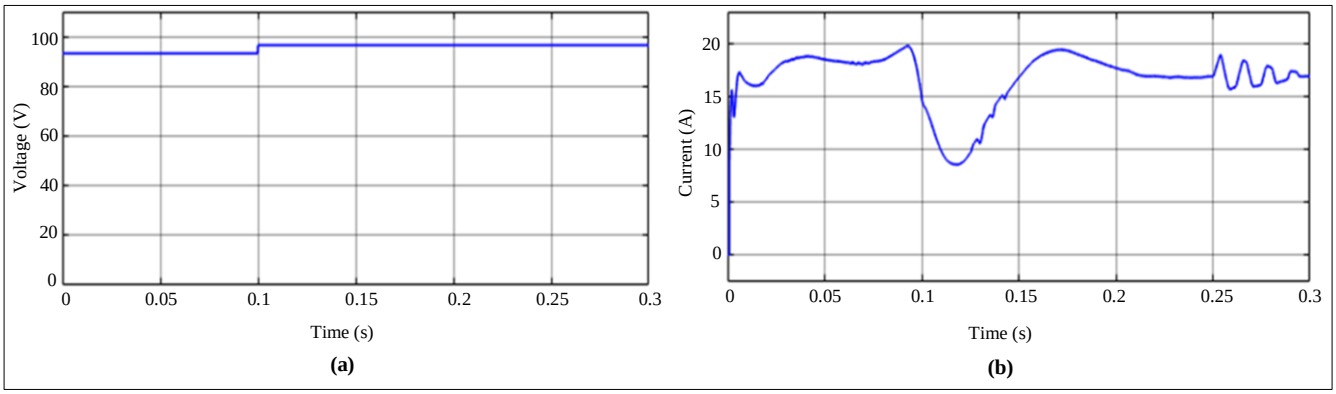

Fig. 10 Solar panel waveform (case 1) (a) Voltage, and (b) Current.

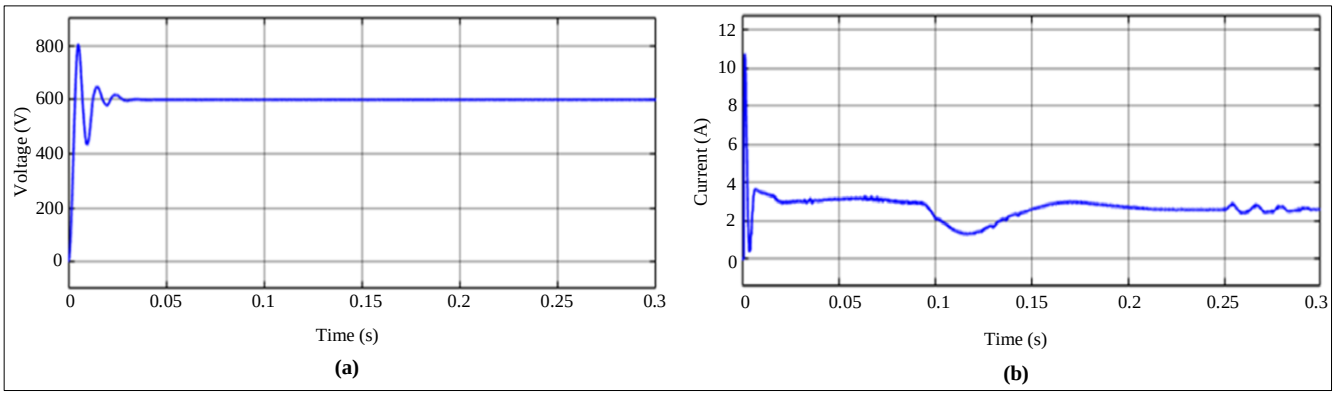

Fig. 11 Converter waveforms (case 1) (a) Output voltage using SLnO-PI controller, and (b) Output current.

The converter waveforms for output voltage using the SLnO-PI controller and converter output current waveforms are illustrated in Figure 11. Using the SLnO-PI controller, distortions are eliminated, and voltage is maintained constantly at 600V throughout the system, as presented in Figure 11(a). The current waveform for the converter is depicted in Figure 11(b), which details that initially current rises above 10A and it gets settles with minor distortions.

4.1.1. Variation in Wind Speed (12m/s-14m/s)

The waveform for wind speed with variation from 12m/s to 14m/s, DFIG output voltage and PWM rectifier output voltage is illustrated in Figure 12. The waveform for wind speed is shown in Figure 12(a), in which 12m/s is maintained constantly till 0.1s, and it is raised to 14m/s after 0.1s, which is continuously maintained throughout the system. Initially, the output voltage of DFIG fluctuates due to the environment, and it is maintained constant within the range of +600 and -600 after 0.1s, as shown in Figure 12(b). PWM rectifier output voltage is raised initially above 400V due to wind gusts, and it is maintained constant at 600V after 0.15s with minor distortions, as shown in Figure 12(c).

The waveforms for the battery are illustrated in Figure 13, in which battery voltage is maintained constant at 24V throughout the system, as indicated in Figure 13(a). The waveform for battery current is illustrated in Figure 13(b), in which the current is raised to peak and continued with small distortions at 1.5A after 0.05s throughout the system. Battery SOC waveform depicted in Figure 13(c) details that 90% of the charge is stored in the battery for further use of EVs.

Figure 14 illustrates the grid voltage, current, and in-phase voltage and current waveforms. The grid voltage is kept within the ±400V range, as Figure 14(a) illustrates. The grid's current waveform is displayed in Figure 14(b), which shows that the system's total current is kept within a ±12A range. The system-wide in-phase voltage and current are depicted in Figure 14(c). The natural and reactive power waveforms are illustrated in Figure 15, in which reactive power is a part of complicated electricity that corresponds to energy being stored and retrieved compared to consumption, which is represented in VAR.

4.2. Case 2: Variation in Intensity and Constant Temperature

The waveforms for temperature and irradiance of solar panel are depicted in Figure 16, in which temperature is continued to be constant at 35℃ throughout this case 2 as shown in Figure 16(a). The waveform for solar irradiation is represented in Figure 16(b), which shows that intensity is sustained at 800W/sq.m; after 0.1s, there is a rise in irradiation, and it is sustained at 1000W/sq-m throughout the system.

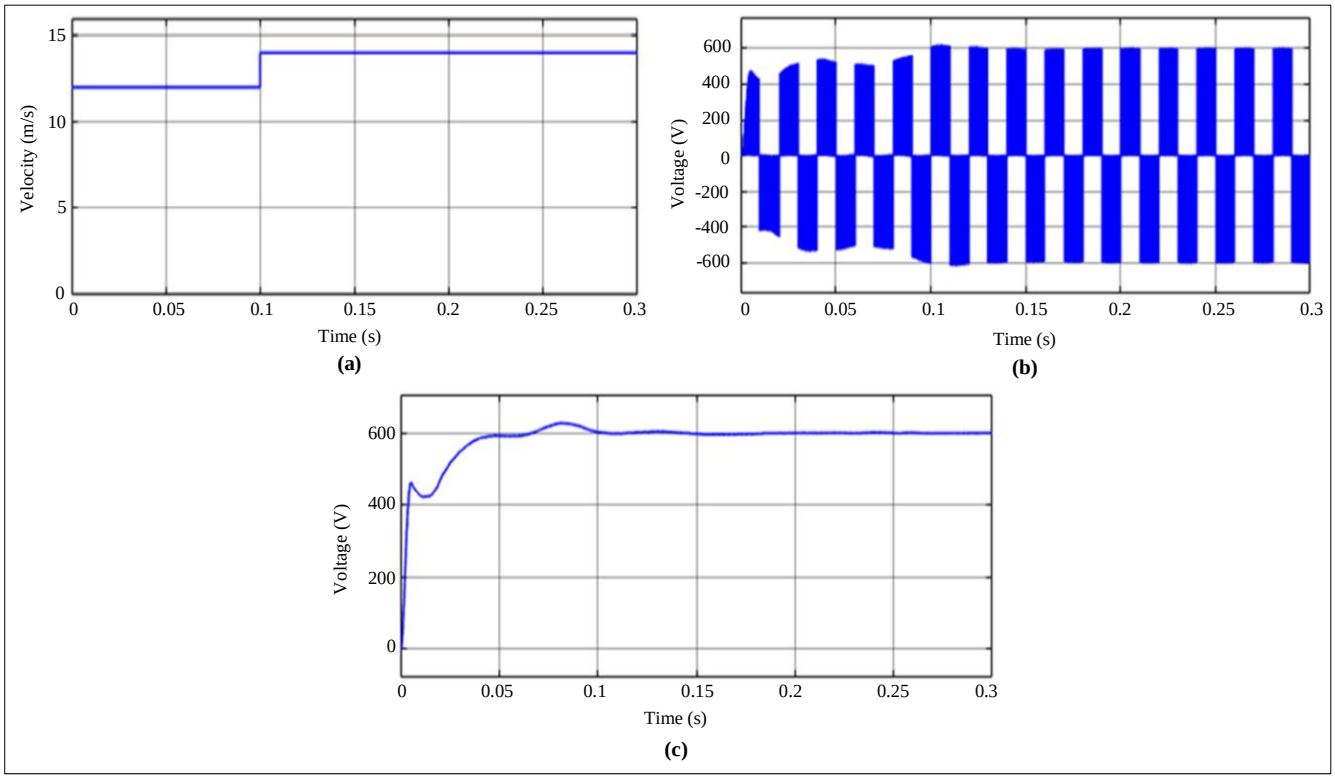

Fig. 12 Waveform (case 1) (a) Wind speed, (b) DFIG output voltage, and (c) PWM rectifier output voltage.

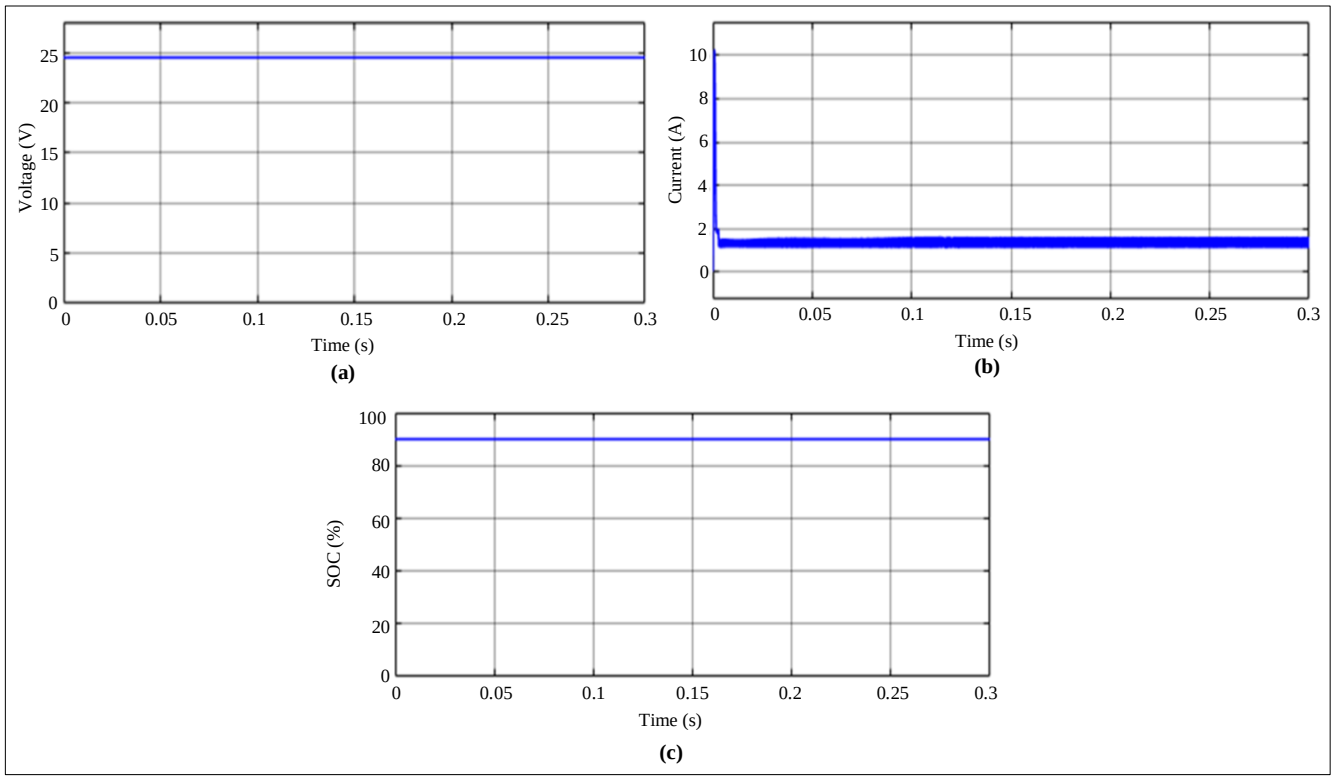

Fig. 13 Battery waveforms (case 1) (a) Voltage, (b) Current, and (c) SOC.

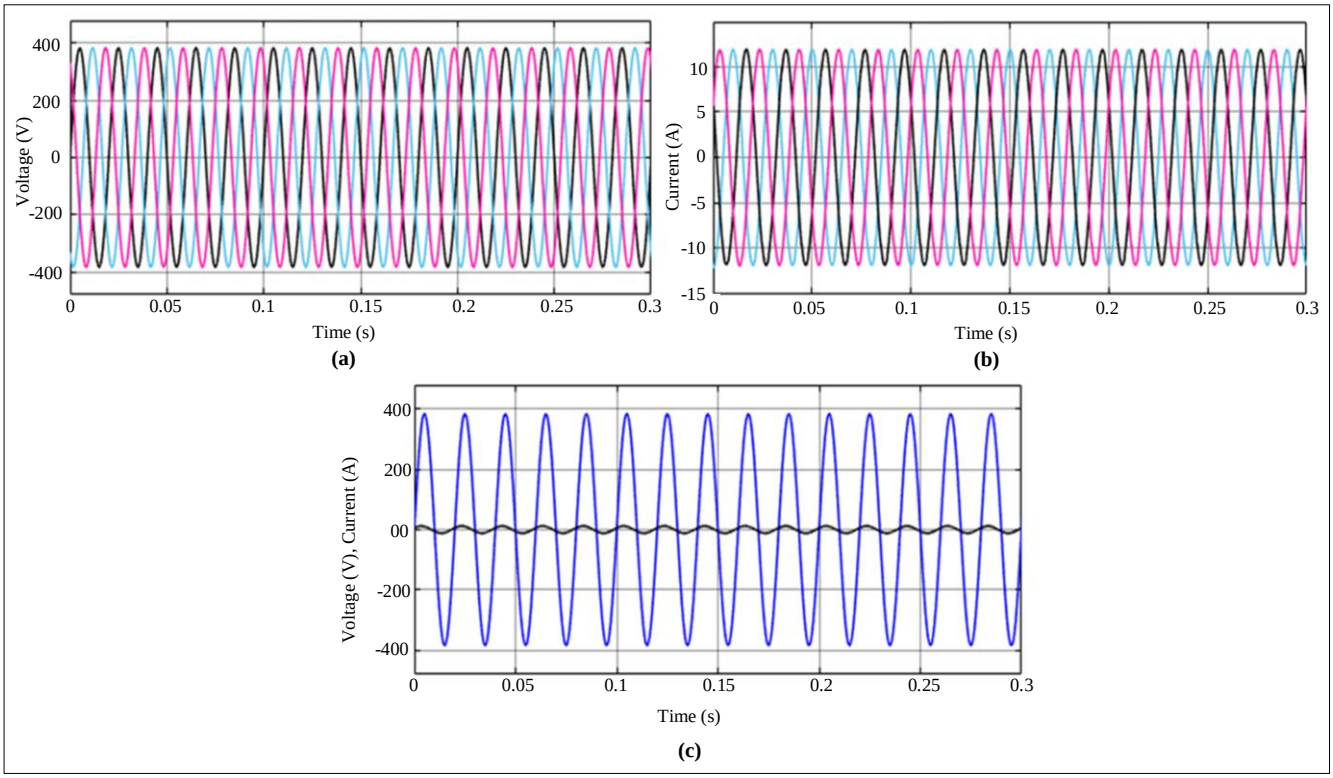

Fig. 14 Grid waveforms (case 1) (a) Voltage, (b) Current, and (c) In-phase voltage and current.

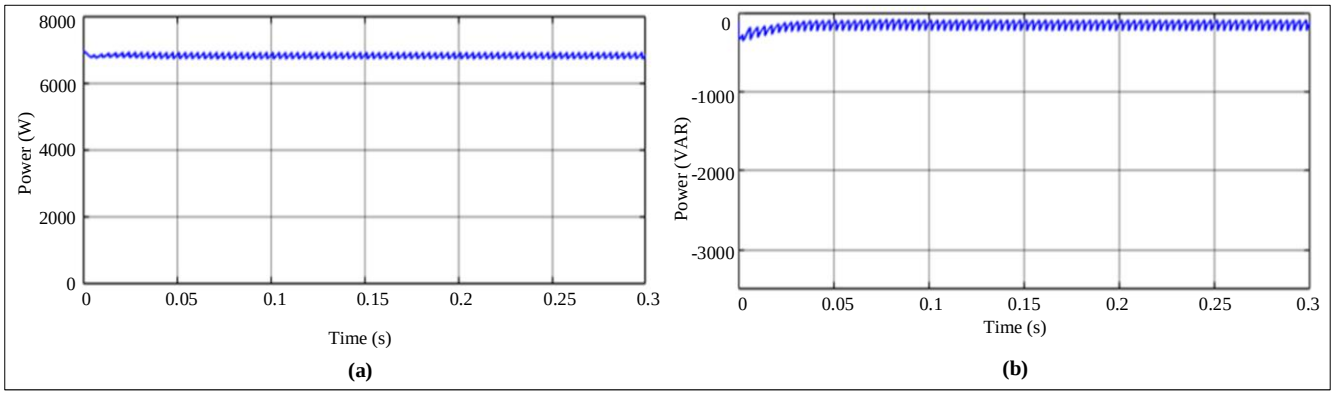

Fig. 15 Waveforms (case 1) (a) Real power, and (b) Reactive power.

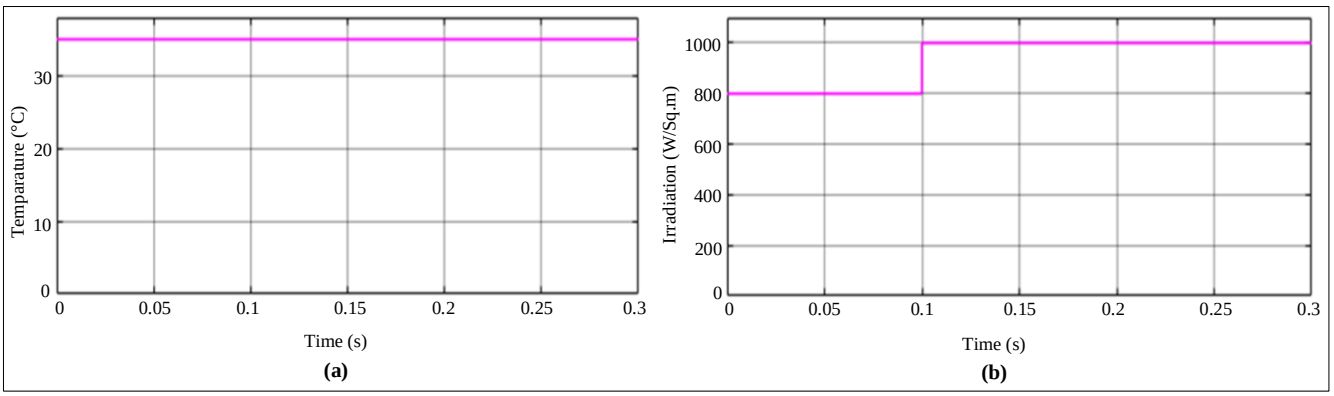

Fig. 16 Solar waveforms (case 2) (a) Constant temperature, and (b) Varying irradiation.

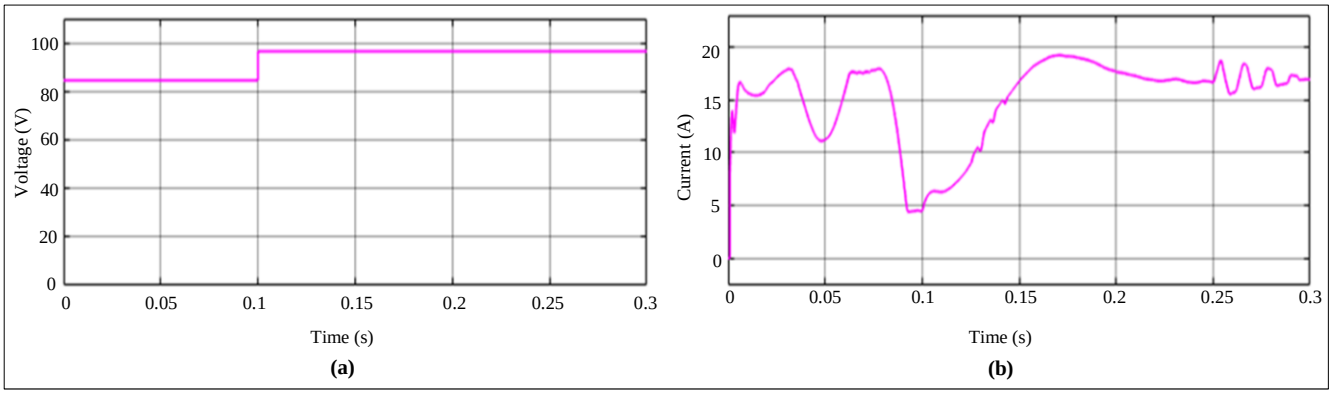

Fig. 17 Solar panel waveforms (case 2) (a) Voltage, and (b) Current.

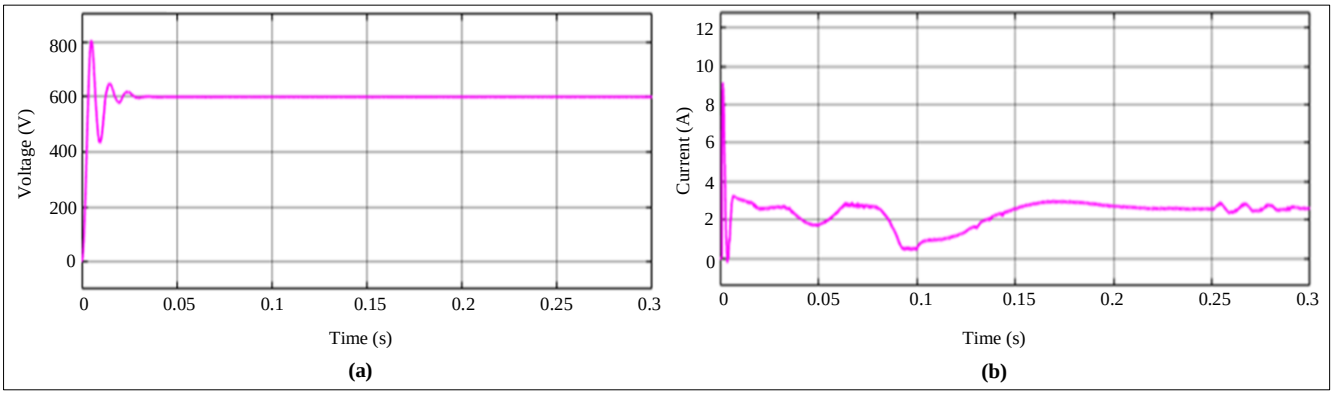

Fig. 18 Converter waveforms (case 2) (a) Voltage using SLnO-PI controller, and (b) Output current.

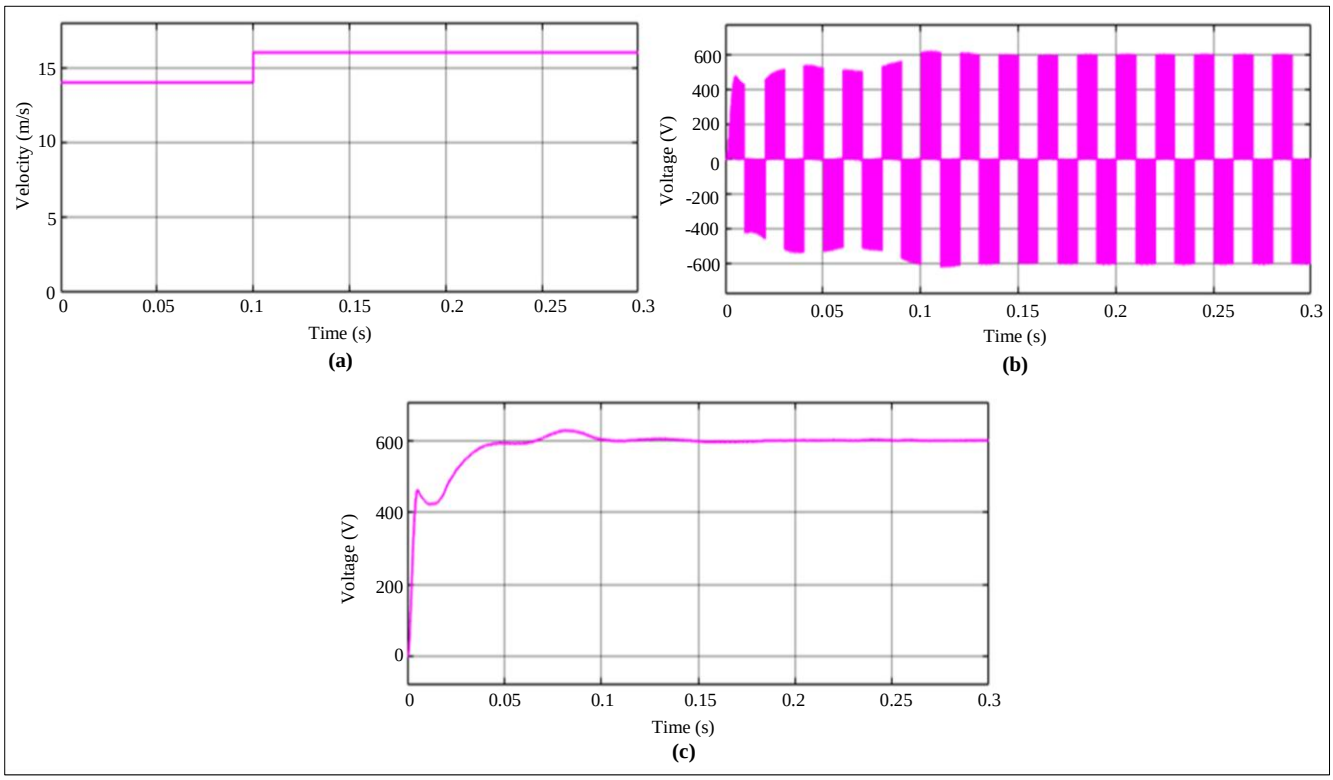

Fig. 19 Waveforms (case 2) (a) Wind speed, (b) DFIG output voltage, and (c) PWM rectifier output voltage.

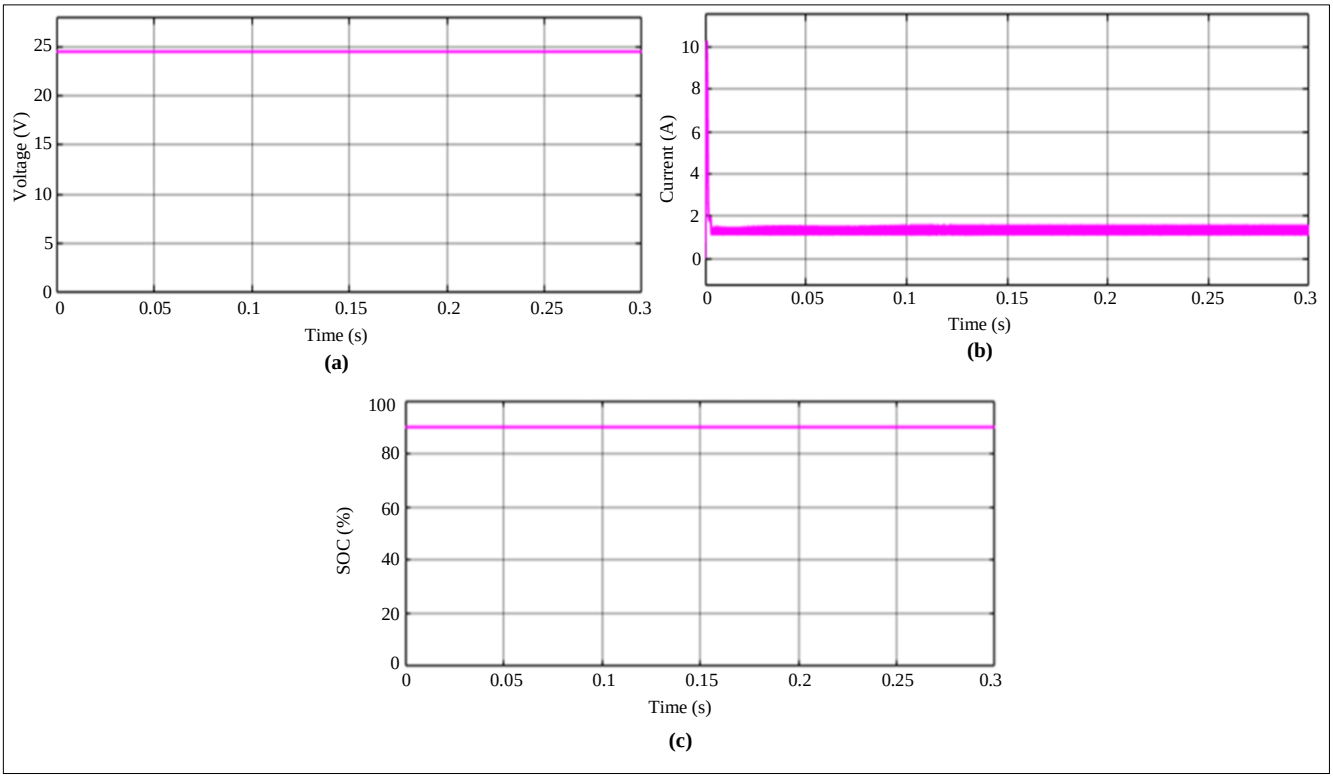

Fig. 20 Battery waveforms (case 2) (a) Voltage, (b) Current, and (c) SOC.

Figure 17 shows the solar panel's voltage and current waveforms, in which the voltage of the panel is steadily maintained at 85V initially and then at 0.1s, the voltage is raised to 95V, which is constantly held throughout the system as illustrated in Figure 17(a). The current waveform depicted in Figure 17(b) details that the current is raised above 15A and fluctuates continuously due to environmental conditions.

The converter output voltage and current waveforms are depicted in Figure 18; by using an SLnO-PI controller, converter output is regulated in which there is a peak rise in the beginning, and it is constantly maintained at 600V throughout the system, as illuminated in Figure 18(a). The current waveform for the converter is illuminated in Figure 18(b), in which the current is raised above 9A initially and settles with minor distortions.

4.2.1. Variation in Wind Speed (14m/s-16m/s)

The following section deals with outcomes obtained by varying the wind speed of DFIG-based WECS from 14m/s to 16m/s. The speed of wind is initially maintained at 14m/s, which is then increased above 15m/s and maintained at 16m/s after 0.1s throughout the system, as depicted in Figure 19(a). The waveform for voltage obtained from DFIG is indicated in Figure 19(b), which shows that the voltage fluctuates initially and gets constant within the range of ±600V after 0.1s. The rectifier output voltage waveform is shown in Figure 19(c), in which voltage is raised above 400V initially, and it is kept steady at 600V after 0.15s.

The waveforms for the battery are depicted in Figure 20, in which the voltage of the battery is maintained at 24V throughout the system, as illustrated in Figure 20(a). The battery current waveform is initially raised to 10A, and then it settles down at 1.5A with minor distortions, as shown in Figure 20(b). The waveform for battery SOC is shown in Figure 20(c), which represents that 90% of charge is held in the battery, which is further used by EVs when the PV panel loses its power during night time.

The grid waveforms for voltage, current and in-phase voltage and current are illuminated in Figure 21. The voltage waveform for the grid is illuminated in Figure 21(a), in which voltage is varied within the limit of ±400V throughout the system. The current waveform for the grid, illustrated in Figure 21(b), details that the current is varied within the range of ±12A. Figure 21(c) demonstrates that voltage and current are in phase throughout the system.

Figure 22 shows waveforms of reactive and real power. Reactive power, which is a component of complicated electricity, corresponds to the energy that is stored and recovered as compared to consumption, which VAR represents. Watts is employed to describe actual power used or consumed in an alternating current circuit. Real and reactive power waveforms are shown in Figure 22. When compared to consumption, which is represented by VAR, reactive power, which is a component of complex electricity, corresponds to energy that is saved and recovered.

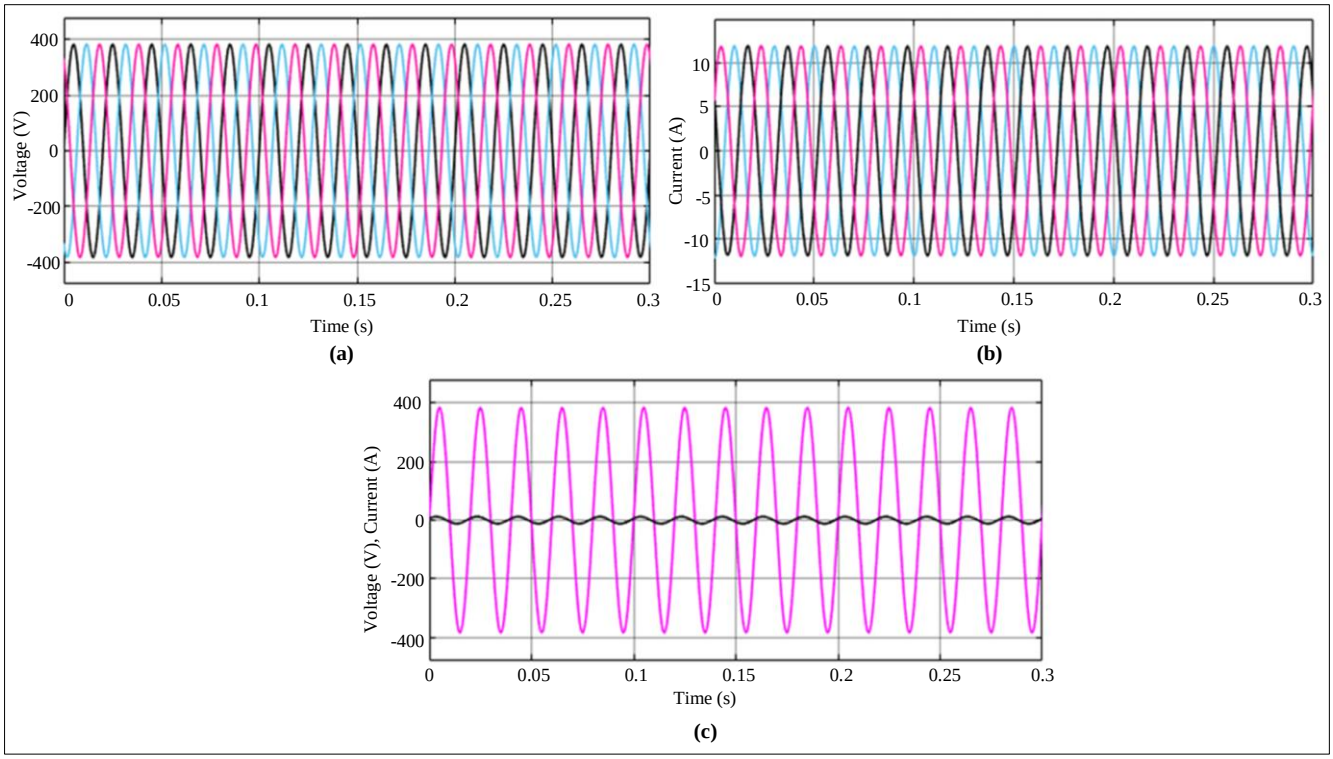

Fig. 21 Grid waveforms (case 2) (a) Voltage, (b) Current, and (c) Voltage and current in-phase waveform.

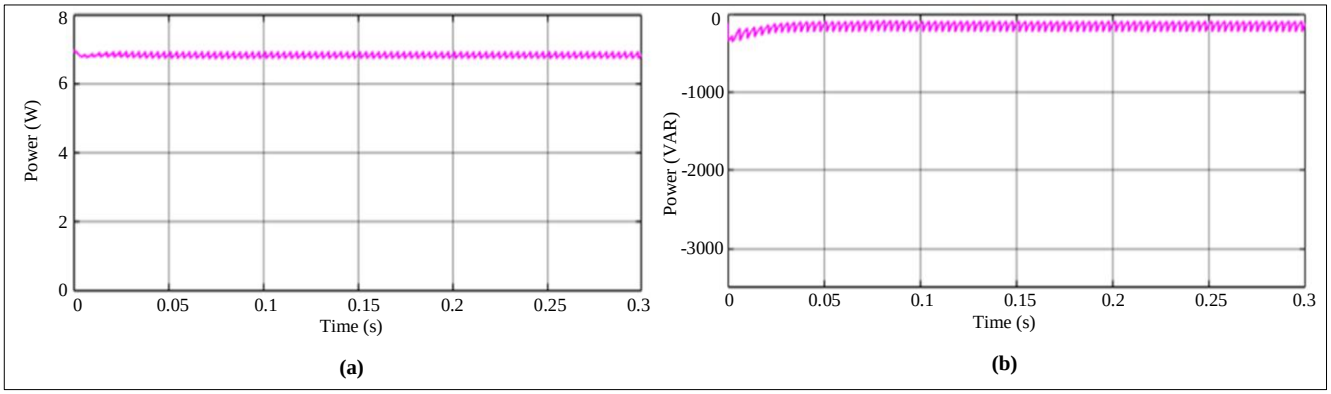

Fig. 22 Waveforms (case 2) (a) Real power, and (b) Reactive power.

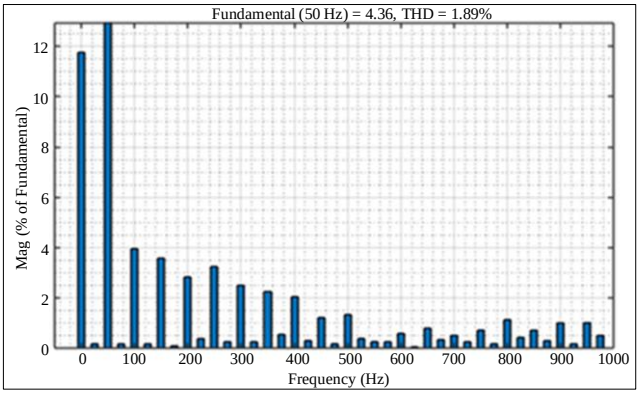

Fig. 23 THD waveform

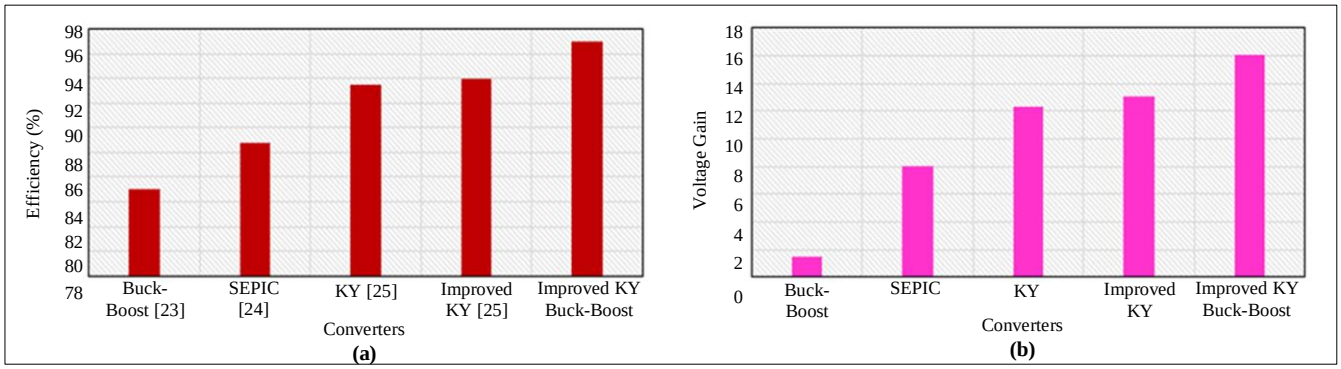

Fig. 24 Comparison graph (a) Efficiency, and (b) Voltage gain.

Table 2. Comparison of efficiency and voltage gain of different converters

Converter	Efficiency (%)	Voltage Gain
Buck-Boost [23]	85	1.5
SEPIC [24]	88.82	8
KY [25]	93.54	12.33
Improved KY [25]	94	13
Improved KY Buck-Boost	97	16

Table 3. Comparison of different controllers

Control Approaches	Settling Time (s)	Rise Time (s)	Peak Time (s)
PI [22]	-	0.01	0.1
SLnO-PI	0.05	0.01	0.1

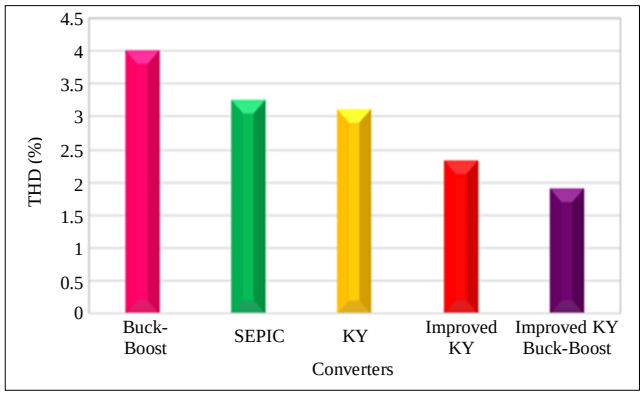

Fig. 25 Comparison of THD output

The graphical demonstration of THD output is depicted in Figure 23. It represents the degree of modification in the output waveform. THD influences the power system because it results from any deviation in the sinusoidal waveform produced by PWM when compared to other arrangements; the proposed converter exhibits reduced harmonic distortion with 1.89%, further reduced by using a filter over the load. The comparison graph for efficiency and voltage gain is illustrated in Figure 24 and Table 2, in which it is compared for conventional converters such as Buck-Boost, SEPIC, KY, Improved KY, and improved KY buck-boost converter with efficiency of 85%, 88.82%, 93.54%, 94% and 97%.

From the comparison graph, it is observed that the improved KY buck boost converter has better efficiency, which improves the performance of the system, as shown in Figure 24(a). As can be seen in Figure 24(b), the proposed converter obtains a maximum voltage gain of 1:16 in the voltage gain comparison. Table 3 indicates a comparison of the peak time, rise time and settling time of PI and SLnO-PI controller approaches, in which it is clear that the proposed approach has better performance that settles at 0.05s, thereby improving the effectiveness of the system. The comparison for THD output is illustrated in Figure 25, which is compared for Buck-Boost, SEPIC, KY, Improved KY and improved KY buck-boost converter. The proposed converter has a THD value of 1.89% which is lesser than other conventional converters.

5. Conclusion

EV usage has been increasing rapidly due to its reduction in greenhouse gas emissions, advance of air quality and decline of climate impact in urban areas due to its use of electricity instead of fossil fuels such as diesel and petrol. An EV battery charging system powered by solar power is designed for clean and stable charging during long-distance travel. At the same time, excess energy is stored in EV batteries for future use. In this work, an improved KY buck-boost converter is utilized for the enhancement of DC voltage obtained from the PV system. The SLnO-based PI controller is being used due to the fact that it has a rapid speed of convergence with a smaller number of iterations and a more effective damping characteristic. The 3ϕ VSI is controlled by a PI controller, which synchronizes the grid with a THD of 1.89%. The simulation in MATLAB software yields an efficiency of 97% and a voltage gain of 1:16 for the proposed converter.

References

[1] Aswad Adib et al., "E-Mobility-Advancements and Challenges," *IEEE Access*, vol. 7, pp. 165226-165240, 2019. [CrossRef] [Google Scholar] [Publisher Link]

[2] S. Sheik Mohammed et al., "Interruptible Charge Scheduling for Plug-In Electric Vehicle to Minimize Charging Cost Using Heuristic Algorithm," *Electrical Engineering*, vol. 104, pp. 1425-1440, 2021. [CrossRef] [Google Scholar] [Publisher Link]

[3] Sheik Mohammed S. et al., "Charge Scheduling Optimization of Plug-In Electric Vehicle in a PV Powered Grid-Connected Charging Station Based on Day-Ahead Solar Energy Forecasting in Australia," *Sustainability*, vol. 14, no. 6, pp. 1-20, 2022. [CrossRef] [Google Scholar] [Publisher Link]

[4] Azuka Affam et al., "A Review of Multiple Input DC-DC Converter Topologies Linked with Hybrid Electric Vehicles and Renewable Energy Systems," *Renewable and Sustainable Energy Reviews*, vol. 135, 2021. [CrossRef] [Google Scholar] [Publisher Link]

[5] Samuel C. Johnson, Joshua D. Rhodes, and Michael E. Webber, "Understanding the Impact of Non-Synchronous Wind and Solar Generation on Grid Stability and Identifying Mitigation Pathways," *Applied Energy*, vol. 262, 2020. [CrossRef] [Google Scholar] [Publisher Link]

[6] Samuel C. Johnson et al., "Evaluating Rotational Inertia as a Component of Grid Reliability with High Penetrations of Variable Renewable Energy," *Energy*, vol. 180, pp. 258-271, 2019. [CrossRef] [Google Scholar] [Publisher Link]

[7] Mummadi Veerachary, and Punit Kumar, "Analysis and Design of Quasi-Z-Source Equivalent DC-DC Boost Converters," *IEEE Transactions on Industry Applications*, vol. 56, no. 6, pp. 6642-6656, 2020. [CrossRef] [Google Scholar] [Publisher Link]

[8] Shan Miao, and Jinfeng Gao, "A Family of Inverting Buck-Boost Converters with Extended Conversion Ratios," *IEEE Access*, vol. 7, pp. 130197-130205, 2019. [CrossRef] [Google Scholar] [Publisher Link]

[9] Aniket Anand, and Bhim Singh, "Modified Dual Output Cuk Converter-Fed Switched Reluctance Motor Drive with Power Factor Correction," *IEEE Transactions on Power Electronics*, vol. 34, no. 1, pp. 624-635, 2019. [CrossRef] [Google Scholar] [Publisher Link]

[10] Radha Kushwaha, and Bhim Singh, "A Power Quality Improved EV Charger with Bridgeless Cuk Converter," *IEEE Transactions on Industry Applications*, vol. 55, no. 5, pp. 5190-5203, 2019. [CrossRef] [Google Scholar] [Publisher Link]

[11] Binxin Zhu et al., "Single-Switch High Step-Up Zeta Converter Based on Coat Circuit," *IEEE Access*, vol. 9, pp. 5166-5176, 2021. [CrossRef] [Google Scholar] [Publisher Link]

[12] Yam P. Siwakoti et al., "High-Voltage Gain Quasi-SEPIC DC-DC Converter," *IEEE Journal of Emerging and Selected Topics in Power Electronics*, vol. 7, no. 2, pp. 1243-1257, 2019. [CrossRef] [Google Scholar] [Publisher Link]

[13] Pandav Kiran Maroti et al., "A New Structure of High Voltage Gain SEPIC Converter for Renewable Energy Applications," *IEEE Access*, vol. 7, pp. 89857-89868, 2019. [CrossRef] [Google Scholar] [Publisher Link]

[14] K. Ramash Kumar et al., "Comprehensive Review of KY Converter Topologies, Modulation and Control Approaches with Their Applications," *IEEE Access*, vol. 10, pp. 20978-20994, 2022. [CrossRef] [Google Scholar] [Publisher Link]

[15] G. Saritha, and D. Kirubakaran, "Design and Implementation of KY Buck-Boost Converter with Voltage Mode Control," *International Journal of Engineering and Advanced Technology*, vol. 8, no. 5, pp. 527-531, 2019. [Google Scholar] [Publisher Link]

[16] Namon Kunjittipong, Kuagoon Kongkanjana, and Sudarat Khwan-on, "Comparison of Fuzzy Controller and PI Controller for a High Step-Up Single Switch Boost Converter," *2020 3rd International Conference on Power and Energy Applications (ICPEA)*, Busan, Korea (South), pp. 94-98, 2020. [CrossRef] [Google Scholar] [Publisher Link]

[17] Sourabh Katoch, Sumit Singh Chauhan, and Vijay Kumar, "A Review on Genetic Algorithm: Past, Present, and Future," *Multimedia Tools Applications*, vol. 80, pp. 8091-8126, 2021. [CrossRef] [Google Scholar] [Publisher Link]

[18] Ravindra Kumar Yadav, P.N. Hrisheekesha, and Vikas Singh Bhadoria, "Grey Wolf Optimization Based Demand Side Management in Solar PV Integrated Smart Grid Environment," *IEEE Access*, vol. 11, pp. 11827-11839, 2023. [CrossRef] [Google Scholar] [Publisher Link]

[19] Jon Martinez-Rico et al., "Multi-Objective Optimization of Production Scheduling Using Particle Swarm Optimization Algorithm for Hybrid Renewable Power Plants with Battery Energy Storage System," *Journal of Modern Power Systems and Clean Energy*, vol. 9, no. 2, pp. 285-294, 2021. [CrossRef] [Google Scholar] [Publisher Link]

[20] Rajeshkumar M. Prasad, and Mahmadasraf A. Mulla, "Rotor Position-Sensorless Algorithms for Direct Power Control of Rotor-Tied DFIG," *IEEE Transactions on Power Electronics*, vol. 36, no. 6, pp. 6213-6217, 2021. [CrossRef] [Google Scholar] [Publisher Link]

[21] Hooman Mohammadi Moghadam et al., "A Novel Supervised Control Strategy for Interconnected DFIG-Based Wind Turbine Systems: MiL Validations," *IEEE Transactions on Emerging Topics in Computational Intelligence*, vol. 5, no. 6, pp. 962-971, 2021. [CrossRef] [Google Scholar] [Publisher Link]

[22] Xiaodong Liang, and Chowdhury Andalib-Bin-Karim, "Harmonics and Mitigation Techniques through Advanced Control in Grid-Connected Renewable Energy Sources: A Review," *IEEE Transactions on Industry Applications*, vol. 54, no. 4, pp. 3100-3111, 2018. [CrossRef] [Google Scholar] [Publisher Link]

[23] Mohamad Reza Banaei, and Hossein Ajdar Faeghi Bonab, "A High Efficiency no Isolated Buck-Boost Converter Based on ZETA Converter," *IEEE Transactions on Industrial Electronics*, vol. 67, no. 3, pp. 1991-1998. [CrossRef] [Google Scholar] [Publisher Link]

[24] Bhim Singh, and Radha Kushwaha, "A PFC Based EV Battery Charger Using a Bridgeless Isolated SEPIC Converter," *IEEE Transactions on Industry Applications*, vol. 56, no. 1, pp. 477-487, 2020. [CrossRef] [Google Scholar] [Publisher Link]

[25] Ilambirai Raghavan Chandran et al., "Implementation of Non-Isolated Zeta-ky Triple Port Converter for Renewable Energy Applications," *Electronics*, vol. 10, no. 14, pp. 1-28, 2021. [CrossRef] [Google Scholar] [Publisher Link]